Research Square

Preprints are preliminary reports that have not undergone peer review.
They should not be considered conclusive, used to inform clinical practice,
or referenced by the media as validated information.

Tiny selective perturbations control violent eruptions without stabilising fusion plasma

SeongMoo Yang

syang@pppl.gov

Princeton Plasma Physics Laboratory https://orcid.org/0000-0003-1214-1268

SangKyeun Kim

Princeton Plasma Physics Laboratory https://orcid.org/0000-0002-0701-8962

Jong-Kyu Park

Seoul National University

Jaehyun Lee

Korea Institute of Fusion Energy

Minjun Choi

Korea Institute of Fusion Energy https://orcid.org/0000-0002-2825-6484

Qiming Hu

Princeton Plasma Physics Laboratory https://orcid.org/0000-0002-8877-4988

Jaewook Kim

Korea Institute of Fusion Energy

Jekil Lee

Korea Institute of Fusion Energy https://orcid.org/0000-0002-1252-7075

Wonha Ko

Korea Institute of Fusion Energy https://orcid.org/0009-0001-4409-5449

YoungMu Jeon

Korea Institute of Fusion Energy

Gunyoung Park

Korea Institute of Fusion Energy

GyungJin Choi

Korea Advanced Institute of Science & Technology

Taik Soo Hahm

Seoul National University

Yong-Su Na

Seoul National University https://orcid.org/0000-0001-7270-3846

Nikolas Logan

Columbia University

Jongsoo Yoo

Princeton Plasma Physics Laboratory https://orcid.org/0000-0003-3881-1995

Hantao Ji

Princeton University https://orcid.org/0000-0001-9600-9963

Seung-Hoe Ku

Princeton Plasma Physics Laboratory

Alessandro Bortolon

Princeton Plasma Physics Laboratory

Rajesh Maingi

Princeton Plasma Physics Laboratory

Joseph Snipes

Princeton Plasma Physics Laboratory

Physical Sciences - Article

Keywords:

Posted Date: June 5th, 2026

DOI: https://doi.org/10.21203/rs.3.rs-9694297/v1

License: This work is licensed under a Creative Commons Attribution 4.0 International License.
Read Full License

Additional Declarations: There is **NO** Competing Interest.

Tiny selective perturbations control violent eruptions without stabilising fusion plasma

S. M. Yang[1*†], S. K. Kim[1†], J.-K. Park[2*], J. Lee[3], M. J. Choi[3], Q. Hu[1], J. W. Kim[3], J. K. Lee[3], W. H. Ko[3], Y. M. Jeon[3], G. Y. Park[3], G. J. Choi[4], T. S. Hahm[2], Y.-S. Na[2], N. C. Logan[5], J. Yoo[1], H. Ji[1], S. Ku[1], A. Bortolon[1], R. Maingi[1], J. A. Snipes[1]

[1]Princeton Plasma Physics Laboratory, Princeton, NJ, USA.
[2]Seoul National University, Seoul, Republic of Korea.
[3]Korea Institute of Fusion Energy, Daejeon, Republic of Korea.
[4]Korea Advanced Institute of Science and Technology, Daejeon, Republic of Korea.
[5]Columbia University, New York, NY, USA.

*Corresponding author(s). E-mail(s): syang@pppl.gov; jkpark@snu.ac.kr;
†These authors contributed equally to this work.

Abstract

Systems driven far from equilibrium are often unstable and prone to violent bursts, from hurricanes and turbulent flows to fusion plasmas. Although stabilisation can mitigate such events, it often requires substantial energy and is not always practical. Yet guiding such systems into less destructive states without suppressing their underlying drive remains a central challenge in nonequilibrium science [1, 2]. Tokamak fusion plasmas provide an important example because controlling energy release is essential for fusion power production [3, 4]. Their eruptions can impose heat loads exceeding 1 GW $\mathbf{m^{-2}}$ on reactor walls [5], yet can be suppressed by magnetic perturbations of order 0.1% of the confining field strength [6–8]. For over two decades, tokamak experiments have raised a specific question within this broader problem: can such minute perturbations change the macroscopic state without primarily reducing the drive? [8–10] Here, we show that a small spatially patterned magnetic perturbation drives state switching between violent eruptions and gradual dissipation in a fusion plasma. By coordinating the motion of interacting plasma structures, the perturbation

strengthens nonlinear interaction and promotes transfer into broadband turbulence. We directly resolve this transfer pathway in a narrow spatial region, and nonlinear simulations reproduce the same structure while showing that the plasma remains unstable. These results support redistribution of energy release rather than simple stabilisation. More broadly, our results suggest a general control principle for far-from-equilibrium dynamics: rather than overpowering the instability, an appropriately structured perturbation can redirect energy release by synchronising interacting structures and strengthening their nonlinear interaction.

Introduction

A common danger in hurricanes [11], volcanic eruptions [12] and fusion plasmas [4, 13, 14] is not simply how much energy they store, but how rapidly and intensely that energy can be released. Because these systems are continuously supplied with energy, they remain far from thermodynamic equilibrium; in many cases, this drive cannot simply be switched off. A more attractive possibility is therefore to keep the system strongly driven while steering the pathway through which energy is released. A more fundamental obstacle, however, is that far-from-equilibrium systems can select among distinct self-organised release states, yet no general principle predicts which state will emerge or how that selection can be changed [1, 2]. This raises a sharper question: can a perturbation far too weak to reduce the drive nevertheless switch the way a strongly driven system releases its energy?

Tokamak fusion plasmas provide a uniquely controlled setting in which to address this question. They are strongly driven laboratory systems that sustain turbulence and multiscale interactions under reproducible conditions. At the same time, they allow precisely applied external perturbations and measurements at multiple locations, making it possible to isolate cause and effect. The question is also central to fusion energy. A plasma heated toward fusion conditions must release the energy it receives. If this energy escapes gradually through the edge, the plasma can remain hot enough for fusion while keeping wall heat loads manageable [4, 15, 16]. If it escapes explosively through edge-localized modes (ELMs) [3], the wall is struck by transient heat loads that can exceed 1 GW m^{-2} [5].

Remarkably, a tiny externally applied three-dimensional distortion of the magnetic field, only of order 0.1% of the main field, can switch the plasma between these two outcomes [6–8, 17–19]. This perturbation, known as a resonant magnetic perturbation (RMP), is one of the leading methods for ELM suppression. Yet despite extensive experimental and modelling work, how such a weak perturbation prevents explosive energy release remains elusive. One possibility is that it simply prevents the narrow high-pressure pedestal at the plasma edge from reaching the conditions for eruption [20]. Another, more intriguing, possibility is that the plasma remains strongly driven and unstable, but is redirected into a different mode of energy release [10, 21–24].

Resolving this distinction requires measurements that capture the three-dimensional plasma response. Tokamaks are often treated as toroidally symmetric,

but RMPs deliberately break this symmetry and can localize the relevant dynamics to a narrow toroidal sector. Such localized dynamics could be missed by conventional diagnostics that lack toroidal coverage. Previous nonlinear simulations suggested that RMPs suppress ELMs by redirecting the energy of the instability, rather than eliminating the instability itself [10, 21–24]. Yet the critical experimental signature of this mechanism — RMP-synchronised coherent plasma motion accompanied by directional energy transfer away from it — had not been directly observed.

Here we use KSTAR, a tokamak with a highly symmetric magnetic field around the torus [25], to show how this switch occurs. We find that the weak three-dimensional field creates a sharply localized structure confined to a narrow toroidal sector. Around this structure, energy flows away from a coherent structure into continuous broadband fluctuations, instead of building into an eruption. Nonlinear MHD simulations reproduce the transition from eruptions to suppression as the applied perturbation is increased, even when the edge pressure profile is held fixed. Together, these results show that weak three-dimensional magnetic fields suppress violent eruptions by organising a non-eruptive pathway for unstable energy release, not simply by reducing the drive.

Small perturbation switches eruptions into turbulence

A small, carefully tuned magnetic perturbation, applied through coils that create a weak repeating pattern around the tokamak (Fig. 1c), is enough to suppress the ELM eruptions. Before the current reaches the level required to suppress them, ELM eruptions appear as large spikes in the edge D_α light emission, indicating sudden bursts of particles from the plasma to the surrounding wall (Fig. 1a). As we slowly increase the coil current, these signatures vanish abruptly at $t = 6.52\,\mathrm{s}$, marking entry into the suppressed state. On ramp-down, ELMs reappear only after the applied field falls to a value about 10% below the onset threshold, revealing hysteresis in the transition.

Importantly, ELM suppression does not simply quiet the plasma edge. Instead of repeated eruptions, the edge enters a new state characterised by persistent broadband turbulence below about 30 kHz (Fig. 1b), consistent with observations in previous studies [26–28]. The abrupt onset of this state, together with its hysteresis, shows that the transition is not a smooth, reversible reduction of edge activity. This broadband activity suggests that energy is released more continuously through turbulence, rather than through violent ELM eruptions. Within this state, filtered edge-temperature images also reveal a repeating vertical pattern that is clear when viewed from one side of the torus but nearly absent from the opposite side (Fig. 1c), pointing to a localized three-dimensional structure.

Localized structure rotating with perturbation

The broadband turbulence that accompanies ELM suppression does not spread uniformly around the torus. It is concentrated in a single, narrow region. To locate this region, we slowly rotated the applied magnetic perturbation at 0.5 Hz while recording the plasma response at fixed diagnostic locations (Fig. 2a). If the turbulent structure

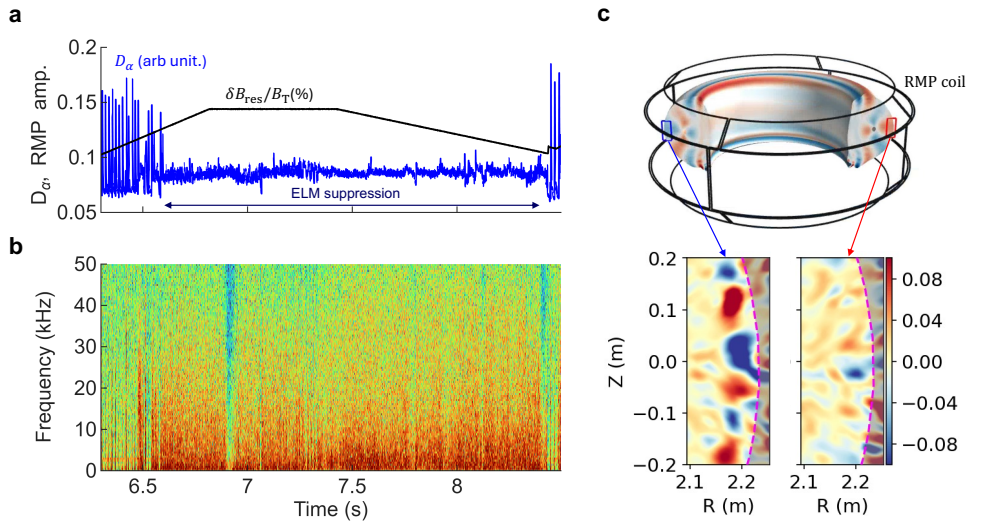


Fig. 1 Transition to a burst-free edge state with a persistent edge structure. a, Applied RMP amplitude, expressed as the resonant field at the pedestal top normalized to the main toroidal field, $\delta B_{res}/B_T$, and the corresponding D_α emission during an RMP scan. Quasi-periodic D_α spikes disappear as the plasma enters a regulated state, and return on ramp-down. Different transition thresholds on ramp-up and ramp-down indicate hysteresis. **b,** Spectrogram of edge fluctuations from the same discharge, showing the accompanying redistribution of spectral power. **c,** Edge structure seen from complementary views. Top, schematic of the viewing geometry, RMP coils and perturbed magnetic-field structure. Bottom, representative snapshots of the 1–30 kHz component of the normalized electron-temperature fluctuation, $\delta T_e/\langle T_e \rangle$, measured from two toroidally opposite views separated by 180°, obtained during a separate matched rotating-RMP discharge. Magenta dashed lines mark the approximate separatrix.

is tied to the applied perturbation, rotating the perturbation should bring the structure across the fixed diagnostic view, allowing us to reconstruct where the activity is concentrated. KSTAR's small pre-existing magnetic imperfections [25] provided a clean setting for rotating the asymmetric perturbation, and ELM suppression persisted throughout three full rotations. These results were independently confirmed by diagnostics at additional locations around the torus (Extended Data Fig. 1, Methods).

The same structure reappears at the same location around the torus with every rotation, consistently over three cycles (Fig. 2c). This shows that the structure is not randomly distributed, but it is anchored to a specific toroidal position that rotates together with the applied perturbation. Away from this region, the edge-temperature activity is strongly reduced. This localization cannot be explained by a perturbation-induced plasma displacement (Extended Data Fig. 3). The T_i variation tracks whether the diagnostic samples a more outward or inward position, but the turbulence enhancement at the same toroidal location occurs between these extrema and only once per RMP cycle, although the same viewing condition recurs twice. The signal, therefore, reflects a localized plasma response rather than a geometric viewing effect.

Strikingly, the nonlinear transfer of energy from low-frequency oscillations (3–9 kHz) to higher-frequency fluctuations (10–30 kHz) decays much more rapidly with position around the torus than the fluctuation amplitude itself (Fig. 2d; Methods). In

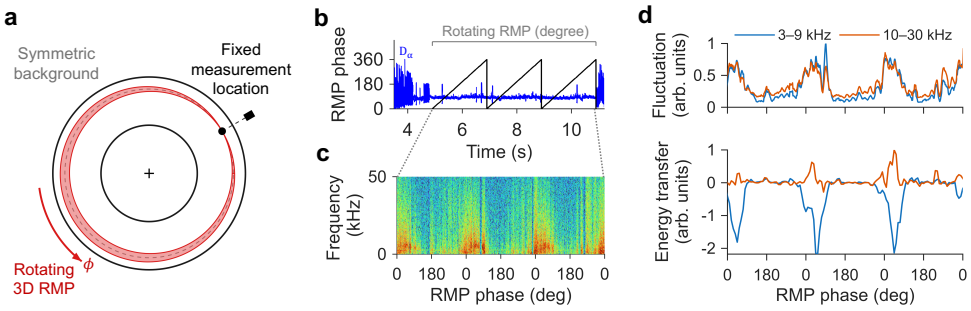


Fig. 2 A hidden 3D interaction region revealed by rotating the RMP. a, Geometry of the rotating 3D RMP and a fixed measurement location. **b,** Applied RMP phase and Dα (arb. unit) trace during the regulated interval. **c,** Phase-resolved spectrogram showing T_e fluctuation amplitude as a function of frequency and RMP phase. **d,** Fluctuation amplitude and inferred nonlinear energy transfer (3–9 kHz and 10–30 kHz) versus RMP phase. As the RMP rotates, the response repeats within a narrow phase sector, enabling a field-aligned three-dimensional reconstruction that would be washed out in a single-point view.

Fig. 2d, position around the torus is expressed as the RMP phase. While the fluctuation amplitude extends broadly with a characteristic decay angle of 65°, the energy transfer collapses exponentially within only 30°, roughly two times more sharply. The much sharper localization of the energy transfer than of the fluctuation amplitude suggests a simple picture: energy is redirected in a small three-dimensional region, and the broader turbulent response spreads outward from there.

Persistent edge structure fuels turbulence

The energy transfer originates from a well-defined, persistent structure within the active region, even after ELM eruptions are suppressed. The power spectrum reveals a distinct 3–9 kHz peak above the broadband turbulence (Fig. 3a), indicating a characteristic low-frequency component. In space, this low-frequency fluctuation is organised around the plasma edge, with a dominant toroidal scale of order $n \sim 10$ (Fig. 3b) [29]. These features show that it is not random broadband turbulence, but an organised edge response that remains active in the suppressed state, consistent with earlier observations [27]. Here, we show that this structure redirects energy into higher-frequency fluctuations through a nonlinear transfer pathway confined to a narrow toroidal sector. This localization helps explain why the pathway was difficult to isolate in earlier measurements.

This pathway becomes clearer in the identified most active sector, where the coherent peak, spatial pattern, and turbulence enhancement all overlap. There, bicoherence-based three-wave coupling analysis (Methods) shows that the 3–9 kHz structure is strongly coupled to fluctuations at 10–30 kHz (Fig. 3c), rather than merely coexisting with them. The inferred transfer direction shows that the low-frequency component ($f < 10$ kHz) feeds energy into higher-frequency turbulence (Fig. 3d and Fig. 2d). The rotating-RMP scan therefore isolates the narrow sector where the coherent structure feeds energy into turbulence, rather than merely mapping where fluctuations are largest.

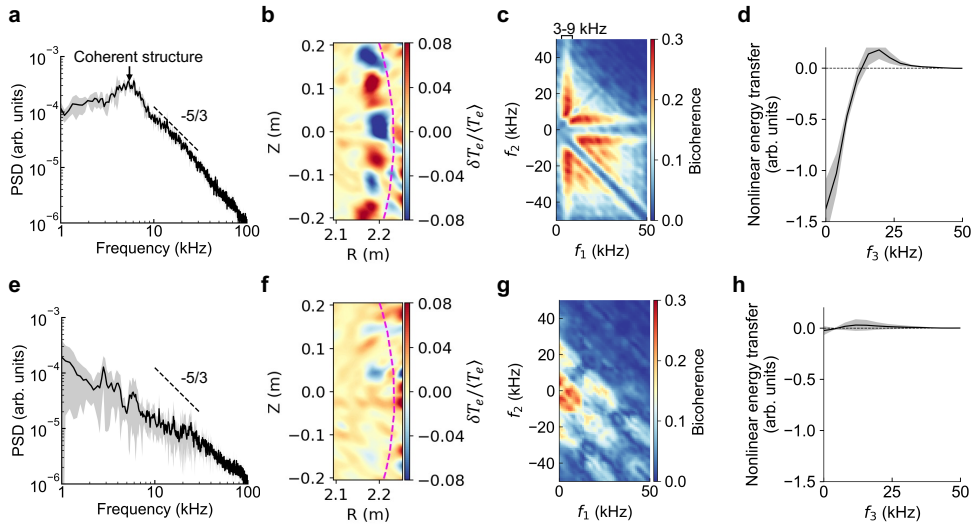


Fig. 3 Nonlinear energy redistribution confined to a narrow RMP phase window. a,e, Power spectra showing a narrow coherent peak on a broadband background (dashed line, $-5/3$ guide). **b,f,** Poloidal cross-sections of band-pass-filtered (3–9 kHz) fluctuations showing a Z-periodic coherent structure in **b** (dashed curve, plasma boundary). **c,g,** Squared bicoherence for phase-coupled triads ($f_3 = f_1 + f_2$), with prominent coupling between $\sim$ 5 kHz and 10–30 kHz bands. **d,h,** Frequency-resolved nonlinear energy-transfer rate. Top row: phase of maximal coupling, where the coherent structure is localized and drives net transfer to higher-frequency fluctuations. Bottom row: 180° shifted phase, where these signatures are absent within measurement sensitivity. Shaded regions indicate the standard deviation across three independent analysis windows

The resulting high-frequency fluctuations form a broadband, roughly power-law spectrum, consistent with redistribution across a range of scales rather than excitation of a few discrete modes [30]. (Fig. 3a; Extended Data Fig. 4). This turbulence turns on abruptly when ELM eruptions vanish (Fig. 1b), suggesting that the two phenomena are closely connected. At a toroidal position 180° away, none of these signatures are observed above the measurement sensitivity (Fig. 3e–h), confirming that the entire process is confined to a narrow toroidal region of the device.

The localized active region poses a critical observational challenge. Because it occupies only a narrow toroidal sector, even modest differences in diagnostic viewing angle can produce very different turbulence signatures. Extended Data Fig. 2 shows that turbulence enhancement can be prominent at some toroidal locations but weak or absent at others, meaning that a diagnostic could miss the active energy-transfer region altogether. This limitation would likely be more severe at higher n, where each active sector is toroidally narrower.

Simulated nonlinear regulation

Nonlinear simulations further distinguish suppression from profile-induced stabilization, where pressure-profile changes keep the plasma below the ELM instability

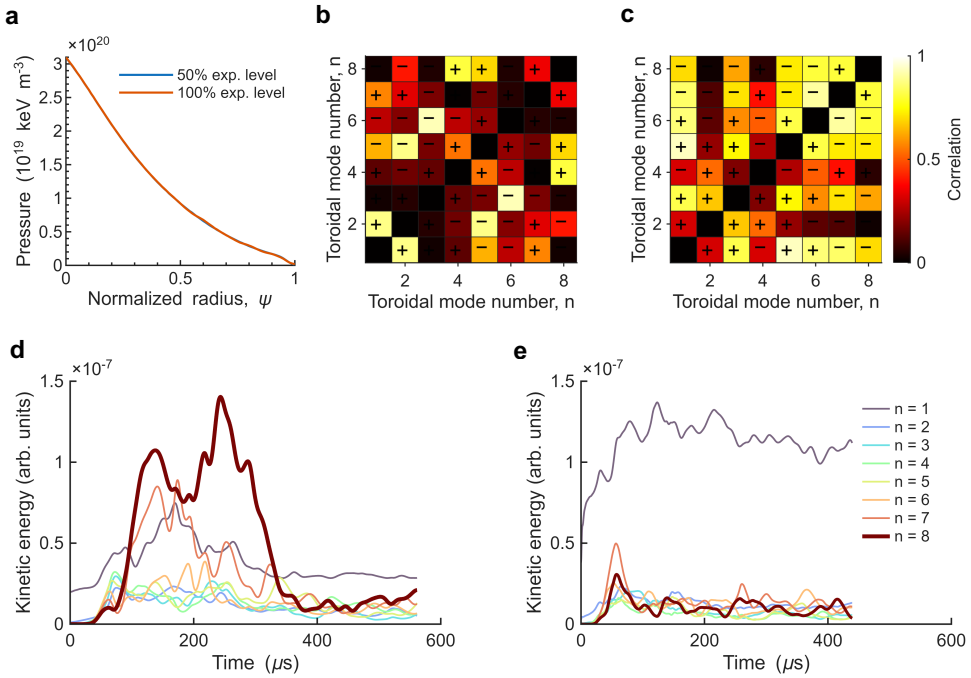


Fig. 4 Matched-profile simulations link eruption control to nonlinear energy redistribution a, Input pressure profiles for the 50% and 100% RMP-amplitude simulations, based on experimental measurements during the ELM-suppressed state. **b,c,** Cross-correlation matrix of mode-resolved kinetic-energy traces, $C(n_1, n_2)$, among toroidal harmonics. The 50% RMP-amplitude case exhibits a sparse correlation pattern, whereas the 100% case shows strong cross-correlations among multiple modes, indicating coordinated inter-mode dynamics. **d,e,** Time evolution of mode-resolved kinetic energy. In the 50% RMP-amplitude case (d), fluctuation energy first concentrates in one dominant toroidal harmonic before abruptly collapsing in an ELM crash. In the 100% RMP-amplitude case (e), energy remains distributed across multiple modes, and no crash is observed.

threshold [20]. Even with the same experimental pressure conditions as in the ELM-suppressed state (Fig. 4a), an eruption still occurs when the perturbation amplitude is reduced by half (Fig. 4d), showing that the outcome is not determined by pressure conditions alone. At the full perturbation amplitude, no eruption occurs (Fig. 4e), even though a small initial disturbance still grows exponentially by eight orders of magnitude. Thus, at fixed pressure drive, instability still develops, but energy release shifts from an eruptive burst to a non-eruptive route organised by the RMP.

The key difference in this instability lies in how energy is released. In the suppressed case, when one mode grows, others weaken, revealing strong interactions among modes (Fig. 4c, 4e). This continuously redistributes energy across many modes, limiting the concentration of energy into a single eruptive structure. In the erupting case, by contrast, these interactions are weak, and energy accumulates in a single dominant mode until it is suddenly released in an eruption (Fig. 4d). These simulations support nonlinear redistribution as the process that prevents eruptions from forming, consistent with the nonlinear energy transfer observed experimentally.

Nonlinear simulations predict that two distinct signatures can emerge when ELM suppression is achieved through nonlinear coupling: a sufficiently large magnetic island at the pedestal top and the synchronisation of the edge structure to the stationary RMP [21–23]. Our measurements reveal both simultaneously. During suppression, the coherent edge structure does not merely slow down; it decelerates, reverses and oscillates about the RMP pattern, indicating that it is effectively synchronised to the applied field (Extended Data Fig. 5, Supplementary Video 1), while a pedestal-top island is present (Extended Data Fig. 3a). At 50% RMP, by contrast, ELMs persist, and nonlinear simulations show that synchronisation is absent under these conditions even with resonant islands. This simultaneous observation supports the simulation picture that a sufficiently large resonant island synchronises the edge modes to the applied 3D field and redirects edge energy away from an eruptive ELM.

Experiments and simulations reveal three signatures of nonlinear regulation in the suppressed state: enhanced fluctuation-energy redistribution, RMP-imposed 3D localization (Extended Data Fig. 3), and RMP-organised coherent-structure motion. This convergence supports the interpretation that both capture the same underlying physics. Together, these results show how a perturbation too small to remove the instability can nevertheless suppress eruption: by redirecting unstable edge energy through a localized three-dimensional nonlinear pathway.

Discussion

Our results show that the observed ELM-suppressed state is not a quiet plasma edge, but a reorganisation of how unstable energy is released. They also provide a unified interpretation of several observations that have often been treated as separate pieces of the RMP ELM-suppression puzzle: magnetic islands [31], enhanced turbulence [26–28] and nonlinear mode coupling [27, 32]. These need not be independent signatures of competing mechanisms, but different manifestations of the same localized three-dimensional plasma response. In this picture, the island structure organises nonlinear energy transfer, enhancing turbulence and diverting energy away from the eruptive pathway. This interpretation does not exclude the RMP-induced profile response; rather, the transition reproduced using a fixed experimental pressure profile shows that profile degradation alone is insufficient to account for suppression.

This localization is not a geometric detail; it is a clue to both the mechanism and its experimental visibility. Previous studies have suggested that magnetic islands can act as localized sources of phase-coupled fluctuations [33]. Our results provide the missing three-dimensional context: the enhanced turbulence is tied to the island structure, but does not simply coincide with a topological landmark such as the island X-point. Instead, the active sector lies closer to where the three-dimensional displacement changes most rapidly [34]. The same localization is reproduced in our nonlinear MHD simulations (Extended Data Fig. 3), supporting the interpretation that the experiment and simulation capture the same underlying physics.

This spatial selectivity has an important diagnostic consequence. A nonlinear process confined to a narrow toroidal sector can appear strong or absent depending on

where it is viewed. Thus, different turbulence signatures reported across RMP experiments may reflect not only different plasma conditions, but also different diagnostic views of a localized three-dimensional nonlinear response.

More broadly, our results point to a different view of violent energy release in magnetized plasmas. A perturbation far too small to suppress the underlying instability can nevertheless redirect unstable energy away from explosive bursts and into a more continuous broadband release pathway. Space plasmas show a similar separation: externally supplied energy can be released either through explosive substorms or through steadier enhanced convection [35]. In space and astrophysical plasmas, magnetic topology, reconnection and turbulence are closely connected to the release of magnetic energy [36]. In such natural systems, however, these processes usually evolve together, making it difficult to isolate how one release pathway is selected over another. Our experiment provides a controlled example in which a magnetic island structure reshapes the pathway of unstable energy release, rather than eliminating the underlying instability.

Beyond magnetized plasmas, however, the underlying principle need not be tied to magnetic geometry itself. What matters is finding a perturbation that couples selectively to the structure or dynamics that determine how an instability releases energy. This points to a central challenge in far-from-equilibrium science: predicting and steering how an unstable driven system selects one self-organised mode of energy release over another [1, 2]. Our results thus provide an experimental demonstration towards a broader physical principle: small structural perturbation can strongly redirect how a much larger instability releases its energy. More generally, steering a strongly driven system may depend less on directly opposing its stored energy than on controlling the structure that shapes its release.

References

[1] Cross, M. C. & Hohenberg, P. C. Pattern formation outside of equilibrium. *Reviews of Modern Physics* **65**, 851–1112 (1993). URL https://link.aps.org/doi/10.1103/RevModPhys.65.851.

[2] Rupe, A. & Crutchfield, J. P. On principles of emergent organization. *Physics Reports* **1071**, 1–47 (2024). URL https://linkinghub.elsevier.com/retrieve/pii/S0370157324001327.

[3] Ham, C., Kirk, A., Pamela, S. & Wilson, H. Filamentary plasma eruptions and their control on the route to fusion energy. *Nature Reviews Physics* **2**, 159–167 (2020). URL https://www.nature.com/articles/s42254-019-0144-1.

[4] Ding, S. *et al.* A high-density and high-confinement tokamak plasma regime for fusion energy. *Nature* **629**, 555–560 (2024). URL https://www.nature.com/articles/s41586-024-07313-3.

[5] Loarte, A. *et al.* Transient heat loads in current fusion experiments, extrapolation to ITER and consequences for its operation. *Physica Scripta* **T128**, 222–228

(2007). URL https://iopscience.iop.org/article/10.1088/0031-8949/2007/T128/043.

[6] Evans, T. E. *et al.* Edge stability and transport control with resonant magnetic perturbations in collisionless tokamak plasmas. *Nature Physics* **2**, 419–423 (2006). URL https://doi.org/10.1038/nphys312.

[7] Park, J. K. *et al.* 3d field phase-space control in tokamak plasmas. *Nature Physics* **14**, 1223–1228 (2018). URL https://doi.org/10.1038/s41567-018-0268-8.

[8] Willensdorfer, M. *et al.* Observation of magnetic islands in tokamak plasmas during the suppression of edge-localized modes. *Nature Physics* **20**, 1980–1988 (2024). URL https://doi.org/10.1038/s41567-024-02666-y.

[9] Evans, T. E. *et al.* Suppression of large edge-localized modes in high-confinement diii-d plasmas with a stochastic magnetic boundary. *Phys. Rev. Lett.* **92**, 235003 (2004). URL https://link.aps.org/doi/10.1103/PhysRevLett.92.235003.

[10] Bécoulet, M. *et al.* Mechanism of Edge Localized Mode Mitigation by Resonant Magnetic Perturbations. *Physical Review Letters* **113**, 115001 (2014). URL https://link.aps.org/doi/10.1103/PhysRevLett.113.115001.

[11] Emanuel, K. A. The dependence of hurricane intensity on climate. *Nature* **326**, 483–485 (1987). URL https://doi.org/10.1038/326483a0.

[12] Woods, A. W. & Koyaguchi, T. Transitions between explosive and effusive eruptions of silicic magmas. *Nature* **370**, 641–644 (1994). URL https://doi.org/10.1038/370641a0.

[13] Kates-Harbeck, J., Svyatkovskiy, A. & Tang, W. Predicting disruptive instabilities in controlled fusion plasmas through deep learning. *Nature* **568**, 526–531 (2019). URL https://doi.org/10.1038/s41586-019-1116-4.

[14] Seo, J. *et al.* Avoiding fusion plasma tearing instability with deep reinforcement learning. *Nature* **626**, 746–751 (2024). URL https://doi.org/10.1038/s41586-024-07024-9.

[15] Han, H. *et al.* A sustained high-temperature fusion plasma regime facilitated by fast ions. *Nature* **609**, 269–275 (2022). URL https://doi.org/10.1038/s41586-022-05008-1.

[16] Na, Y.-S. *et al.* How fast ions mitigate turbulence and enhance confinement in tokamak fusion plasmas. *Nature Reviews Physics* **7**, 190–202 (2025). URL https://doi.org/10.1038/s42254-025-00814-8.

[17] Yang, S. *et al.* Tailoring tokamak error fields to control plasma instabilities and transport. *Nature Communications* **15**, 1275 (2024). URL https://doi.org/10.

1038/s41467-024-45454-1.

[18] Kim, S. K. *et al.* Highest fusion performance without harmful edge energy bursts in tokamak. *Nature Communications* **15**, 3990 (2024). URL https://doi.org/10.1038/s41467-024-48415-w.

[19] Hu, Q. M. *et al.* Taming harmful bursts and heat flux in high-confinement tokamak plasmas. *Nature Communications* **17**, 391 (2025). URL https://doi.org/10.1038/s41467-025-67080-1.

[20] Snyder, P. B. *et al.* The EPED pedestal model and edge localized mode-suppressed regimes: Studies of quiescent H-mode and development of a model for edge localized mode suppression via resonant magnetic perturbations. *Physics of Plasmas* **19**, 056115 (2012). URL https://pubs.aip.org/pop/article/19/5/056115/597019/The-EPED-pedestal-model-and-edge-localized-mode.

[21] Orain, F. *et al.* Non-linear modeling of the threshold between ELM mitigation and ELM suppression by resonant magnetic perturbations in ASDEX upgrade. *Physics of Plasmas* **26**, 042503 (2019). URL https://pubs.aip.org/pop/article/26/4/042503/257071/Non-linear-modeling-of-the-threshold-between-ELM.

[22] Kim, S. *et al.* Nonlinear modeling of the effect of $n = 2$ resonant magnetic field perturbation on peeling-ballooning modes in KSTAR. *Nuclear Fusion* **60**, 026009 (2020). URL https://iopscience.iop.org/article/10.1088/1741-4326/ab5cf0.

[23] Kim, S. *et al.* Nonlinear MHD modeling of n = 1 RMP-induced pedestal transport and mode coupling effects on ELM suppression in KSTAR. *Nuclear Fusion* **62**, 106021 (2022). URL https://iopscience.iop.org/article/10.1088/1741-4326/ac84ef.

[24] Becoulet, M. *et al.* Non-linear MHD modelling of edge localized modes suppression by resonant magnetic perturbations in ITER. *Nuclear Fusion* **62**, 066022 (2022). URL https://iopscience.iop.org/article/10.1088/1741-4326/ac47af.

[25] In, Y., Park, J., Jeon, J., Kim, J. & Okabayashi, M. Extremely low intrinsic non-axisymmetric field in KSTAR and its implications. *Nuclear Fusion* **55**, 043004 (2015). URL https://doi.org/10.1088/0029-5515/55/4/043004.

[26] McKee, G. *et al.* Increase of turbulence and transport with resonant magnetic perturbations in elm-suppressed plasmas on diii-d. *Nuclear Fusion* **53**, 113011 (2013). URL https://doi.org/10.1088/0029-5515/53/11/113011.

[27] Lee, J. *et al.* Nonlinear interaction of edge-localized modes and turbulent eddies in toroidal plasma under $n = 1$ magnetic perturbation. *Phys. Rev. Lett.* **117**, 075001 (2016). URL https://link.aps.org/doi/10.1103/PhysRevLett.117.075001.

[28] Leuthold, N. *et al.* Turbulence characterization during the suppression of edge-localized modes by magnetic perturbations on ASDEX Upgrade. *Nuclear Fusion* **63**, 046014 (2023). URL https://iopscience.iop.org/article/10.1088/1741-4326/acb1c5.

[29] Lee, J. *et al.* Toroidal mode number estimation of the edge-localized modes using the KSTAR 3-D electron cyclotron emission imaging system. *Review of Scientific Instruments* **85**, 063505 (2014). URL https://pubs.aip.org/rsi/article/85/6/063505/355983/Toroidal-mode-number-estimation-of-the-edge.

[30] Frisch, U. *Turbulence: The Legacy of A. N. Kolmogorov* (Cambridge University Press, 1995).

[31] Willensdorfer, M. *et al.* Observation of magnetic islands in tokamak plasmas during the suppression of edge-localized modes. *Nature Physics* **20**, 1980–1988 (2024). URL https://www.nature.com/articles/s41567-024-02666-y.

[32] Choi, M. J. Spectral data analysis methods for the two-dimensional imaging diagnostics (2019). URL https://arxiv.org/abs/1907.09184. arXiv:1907.09184.

[33] Choi, M. J. *et al.* Stochastic fluctuation and transport of tokamak edge plasmas with the resonant magnetic perturbation field. *Physics of Plasmas* **29**, 122504 (2022). URL https://doi.org/10.1063/5.0121690.

[34] Willensdorfer, M. *et al.* Field-line localized destabilization of ballooning modes in three-dimensional tokamaks. *Phys. Rev. Lett.* **119**, 085002 (2017). URL https://link.aps.org/doi/10.1103/PhysRevLett.119.085002.

[35] Sergeev, V. A., Pellinen, R. J. & Pulkkinen, T. I. Steady magnetospheric convection: A review of recent results. *Space Science Reviews* **75**, 551–604 (1996). URL https://doi.org/10.1007/BF00833344.

[36] Ji, H. *et al.* Magnetic reconnection in the era of exascale computing and multiscale experiments. *Nature Reviews Physics* **4**, 263–282 (2022). URL https://www.nature.com/articles/s42254-021-00419-x.

[37] Yang, S. *et al.* Localizing resonant magnetic perturbations for edge localized mode control in kstar. *Nuclear Fusion* **60**, 096023 (2020). URL https://doi.org/10.1088/1741-4326/aba1cf.

[38] Park, J.-k., Boozer, A. H. & Glasser, A. H. Computation of three-dimensional tokamak and spherical torus equilibria. *Physics of Plasmas* **14**, 052110 (2007). URL https://doi.org/10.1063/1.2732170.

[39] Choi, M. J. *et al.* Effects of plasma turbulence on the nonlinear evolution of magnetic island in tokamak. *Nature Communications* **12**, 375 (2021). URL https://doi.org/10.1038/s41467-020-20652-9.

[40] Ritz, C. & Powers, E. Estimation of nonlinear transfer functions for fully developed turbulence. *Physica D: Nonlinear Phenomena* **20**, 320–334 (1986). URL https://www.sciencedirect.com/science/article/pii/0167278986900369.

[41] de Wit, T. D., Krasnosel'skikh, V. V., Dunlop, M. & Lühr, H. Identifying nonlinear wave interactions in plasmas using two-point measurements: A case study of short large amplitude magnetic structures (slams). *Journal of Geophysical Research: Space Physics* **104**, 17079–17090 (1999). URL https://agupubs.onlinelibrary.wiley.com/doi/abs/10.1029/1999JA900134.

[42] Huysmans, G. T. A., Pamela, S., van der Plas, E. & Ramet, P. Non-linear MHD simulations of edge localized modes (ELMs). *Plasma Physics and Controlled Fusion* **51**, 124012 (2009). URL https://iopscience.iop.org/article/10.1088/0741-3335/51/12/124012.

[43] Hoelzl, M. *et al.* The jorek non-linear extended mhd code and applications to large-scale instabilities and their control in magnetically confined fusion plasmas **61**, 065001 (2021). URL https://doi.org/10.1088/1741-4326/abf99f.

[44] Orain, F. *et al.* Non-linear magnetohydrodynamic modeling of plasma response to resonant magnetic perturbations. *Physics of Plasmas* **20**, 102510 (2013). URL http://aip.scitation.org/doi/10.1063/1.4824820.

Methods

KSTAR

KSTAR is a superconducting tokamak at the Korea Institute of Fusion Energy, developed to explore steady-state operating regimes relevant to ITER and future devices. A key advantage for this study is its small intrinsic non-axisymmetric field errors [25]. In many tokamaks, small engineering imperfections (e.g., coil misalignments and manufacturing tolerances) introduce static three-dimensional error fields that distort the magnetic geometry seen by the plasma. In KSTAR, the coil set is located outside the vacuum vessel, which helps reduce the non-axisymmetric error-field components at the plasma. This clean baseline is essential for isolating the localized 3D structures driven by externally applied perturbations from pre-existing background asymmetries.

RMP configuration and ramp protocol

Resonant magnetic perturbations (RMPs) are produced on KSTAR by dedicated external control coils (Fig. 1c), which impose a weak, programmable three-dimensional magnetic perturbation near the plasma edge. In this work, we apply an $n = 1$ perturbation, where n denotes the number of times the imposed magnetic pattern repeats around the torus. Thus, $n = 1$ corresponds to one full period around the torus, the longest-wavelength three-dimensional variation that can be applied. We choose the coil settings to emphasize the edge response while keeping unwanted perturbations of the core as small as possible [17, 37]. This configuration provides robust access to ELM suppression and improves the visibility of the edge-localized three-dimensional structures studied here. The RMP amplitude is slowly ramped up across the ELM-suppression threshold and then ramped back down to test reversibility. This protocol reveals a sharp, switch-like onset of ELM suppression and a clear hysteresis between the up- and down-ramps (Fig. 1). The RMP amplitude in Fig. 1 is expressed as the resonant radial field near the pedestal top, $\delta B_{\mathrm{res}}/B_{\mathrm{T}}$, evaluated at the $q = 5$ surface with IPEC [38]. The linear ideal-MHD plasma response was calculated for a representative time slice in the ELM-suppressed phase and used as a linear calibration between the applied coil current and $\delta B_{\mathrm{res}}/B_{\mathrm{T}}$.

Fluctuation diagnostics

The main fluctuation measurements are based on electron-temperature fluctuations, $\tilde{T}_e$, obtained from electron cyclotron emission imaging (ECEI) diagnostics [27, 29, 39]. Electron cyclotron emission imaging (ECEI) provides time-resolved two-dimensional views of edge temperature-fluctuation structures, which are used to identify the localized patterns discussed in the main text. Density fluctuations, $\tilde{n}$, measured with beam emission spectroscopy (BES), were used as an independent cross-check of the fluctuation dynamics inferred from ECEI. Unless stated otherwise, analyses focus on ECEI channels sampling the pedestal-top vicinity near major radius $R \approx 2.21$ m. The key fluctuation features reported in the main text were consistently observed across multiple discharges.

RMP phase-rotation protocol

The toroidal localization was measured by slowly changing the phase of the applied $n = 1$ RMP during the ELM-suppressed state. Schematically, the applied perturbation may be written as

$$\delta B(\phi, t) \propto A(t) \cos[n\phi + \phi_c(t)],$$

where ϕ is the toroidal angle, $n = 1$, $A(t)$ is the applied perturbation amplitude and $\phi_c(t)$ is the controlled phase. The phase ϕ_c is set electronically through the relative currents in the independently powered KSTAR RMP coils. In practice, the current is distributed among coils located at different toroidal positions; changing their relative currents shifts the phase of the resulting $n = 1$ magnetic pattern. Advancing ϕ_c therefore rotates the perturbation pattern in the laboratory frame while the amplitude is held approximately fixed.

For the phase scan, ϕ_c was advanced at 0.5 Hz. This scan rate is slow compared with the analysed edge fluctuation frequencies, 1–30 kHz, allowing the response to be treated as quasi-steady at each phase. Since the diagnostics are fixed in the laboratory frame, a response tied to the applied perturbation appears strongest at the phase for which the applied pattern passes through the diagnostic view. The phase of maximum response is then used to infer the toroidal location of the response. ELM suppression persisted over three complete rotations, and the inferred localization was cross-checked with diagnostics at additional toroidal locations (Fig. 1).

Nonlinear energy-transfer estimation

We estimated nonlinear spectral energy transfer using a bispectrum-based quadratic transfer-function method [40, 41]. To quantify how the measured fluctuation evolves through nonlinear coupling, we compared the same fluctuation signal over two time intervals separated by a short delay, $\Delta t = 5\,\mu$s. For each Fourier component, this finite-time evolution was represented as a linear response plus quadratic triad interactions,

$$Y_p = L_p X_p + \sum_{\substack{p_1 \geq p_2 \\ p = p_1 + p_2}} Q^p_{p_1,p_2} X_{p_1} X_{p_2}, \tag{1}$$

where X_p and Y_p are the complex Fourier coefficients of the same fluctuation signal evaluated before and after the delay Δt, respectively. Here L_p is the linear transfer function, and $Q^p_{p_1,p_2}$ quantifies quadratic coupling among triads satisfying $p = p_1 + p_2$.

The coefficients were obtained by least-squares fitting over an ensemble of windowed realizations [41]. We used quasi-stationary intervals, 0.1 s analysis windows, $N_{\mathrm{FFT}} = 128$, and 80% overlap. The relatively long analysis window was used to provide sufficient ensemble averaging and to ensure a well-constrained least-squares fit. We also verified that the inferred transfer direction was reproducibly obtained when the analysis was repeated over rotating phases of the perturbation, as shown in Fig. 2d. The fitted quadratic terms were used to estimate nonlinear energy-transfer rates. Under the sign convention used in Fig. 3d, positive and negative values indicate relative energy gain and loss of spectral components through nonlinear coupling, respectively. The transfer-rate spectrum was then integrated over prescribed low- and

high-frequency bands to obtain the phase-resolved summary shown in Fig. 2d and to assess whether the pattern is consistent with low-to-high-frequency energy transfer.

Bicoherence

Broadband fluctuations coincident with ELM suppression suggest enhanced nonlinear interaction, but broadband power alone does not establish nonlinearity because multiple linear modes can superpose to produce a similar spectrum. We therefore use squared bicoherence, which tests whether different frequencies maintain a consistent phase relationship expected for nonlinear three-wave coupling. In the ELM-suppressed state, squared bicoherence exhibits strong coupling among triads satisfying $f_3 = f_1 + f_2$ (Fig. 3c), providing direct evidence of nonlinear interaction beyond random-phase linear superposition.

For a detrended fluctuation signal with Fourier transform $\tilde{X}(f)$, the squared bicoherence is

$$b^2(f_1, f_2) = \frac{\left|\left\langle \tilde{X}^*(f_1+f_2)\,\tilde{X}(f_1)\,\tilde{X}(f_2)\right\rangle\right|^2}{\left\langle\left|\tilde{X}(f_1)\,\tilde{X}(f_2)\right|^2\right\rangle\left\langle\left|\tilde{X}(f_1+f_2)\right|^2\right\rangle}, \tag{2}$$

where $\langle\cdot\rangle$ denotes averaging over windowed segments and * denotes complex conjugation. In practice, $b^2(f_1, f_2)$ was estimated by averaging bispectral products over overlapping segments to improve statistical convergence. Each 0.1-s interval contains 481 windowed FFT segments. The random-phase finite-sample level is therefore of order $1/N_{\mathrm{seg}}$, well below the observed peaks of $b^2 \gtrsim 0.2$, even allowing for reduced independence due to overlap. We also verified that similar bicoherence patterns were reproducibly obtained when the analysis was repeated at different rotating phases of the perturbation within the active region. The bicoherence was evaluated over the same phase interval during three successive rotations of the applied RMP phase, and the displayed map combines the resulting estimates. This confirms that the observed pattern is phase reproducible rather than a chance feature of a single interval.

Nonlinear MHD modelling

To test whether the ELM-suppression threshold is determined by nonlinear dynamics (mode evolution and mode–mode coupling), rather than by slow changes of the mean profiles, we performed nonlinear three-dimensional MHD simulations under experimentally matched conditions ("profile matched"). Specifically, we used the resistive, nonlinear extended MHD code JOREK [42, 43] to model KSTAR experiments with RMPs [44]. The modelling includes a realistic tokamak geometry, a reduced MHD model with two-fluid diamagnetic effects, neoclassical friction, and realistic anisotropies in parallel and perpendicular electron heat transport. In addition, the viscosity ν was set to a realistic value of 1 $\mathrm{m}^2\ \mathrm{s}^{-1}$ in the pedestal region, and the main physical assumption made was equating the ion temperature to the electron temperature ($T_i = T_e$).

Each simulation was initialized from an experimentally reconstructed magnetic equilibrium (EFIT; magnetic equilibrium reconstruction) and the experimentally inferred pressure profiles during an ELM-suppressed state. We then compare two runs that are identical in every respect except for the amplitude of the applied resonant magnetic perturbation (RMP): a full-amplitude case (100%) and a reduced-amplitude case (50%) with the same spatial spectrum and phase. This controlled comparison isolates the effect of the imposed three-dimensional forcing amplitude.

A key element of our methodology is that we focus on the *early-time* response, on timescales much shorter than the characteristic evolution time of the mean profiles. In other words, we examine the dynamics before the background profiles have time to appreciably relax or drift, so that the two cases can be interpreted as starting from (and remaining close to) the same mean state (e.g., profiles). This allows differences between the 100% and 50% cases to be attributed to nonlinear mode dynamics triggered by the forcing amplitude, rather than to gradual profile evolution.

We classify the simulated state as *bursty* or *suppressed* using the dynamical signatures shown in Fig. 4d and 4e. The bursty state is identified by episodes in which fluctuation energy temporarily concentrates into a single toroidal harmonic, followed by a rapid drop of kinetic energy during a crash. The suppressed (regulated) state is identified by the absence of such intermittent crashes, with kinetic energy remaining distributed across multiple harmonics.

To quantify nonlinear coupling among toroidal harmonics, we compute the time-correlation coefficient matrix $C(n_1, n_2)$ of the kinetic energy $W_{\mathrm{kin}}(n)$ for $n = 1$–8. Here $C(n_1, n_2)$ measures how strongly the kinetic-energy time traces of two harmonics rise and fall together over the analysis interval; larger values indicate stronger cross-mode correlation and thus more effective coupling. Finally, to characterize the mode-structure motion, we track the poloidal propagation direction of the dominant perturbations and define oscillatory behaviour by repeated reversals of this direction, rather than steady propagation in a single direction.

Data availability

Raw data were generated by the KSTAR team. The data that support the findings of this study are available from the corresponding author upon reasonable request.

Code availability

The JOREK code is available upon reasonable request to admin@jorek.eu (https://www.jorek.eu).

Acknowledgements

We thank the KSTAR team for experimental and operational support, and the JOREK team for developing and maintaining the JOREK code. We are grateful to M. Hölzl for reviewing the JOREK results, to N. Leuthold for discussions on the applicability of this framework to other devices, and to E. Panov for discussions on whether steady magnetospheric convection (SMC) provides a useful analogy for this work.

Funding

This material was supported by the U.S. Department of Energy under DE-AC02-09CH11466 (Princeton Plasma Physics Laboratory), the Technology Development Projects for Leading Nuclear Fusion through the National Research Foundation of Korea (NRF) funded by the Ministry of Science and ICT (No. RS-2023-00281276), and the New Faculty Startup Fund from Seoul National University in South Korea. The United States Government retains a non-exclusive, paid-up, irrevocable, world-wide license to publish or reproduce the published form of this manuscript or allow others to do so for United States Government purposes.

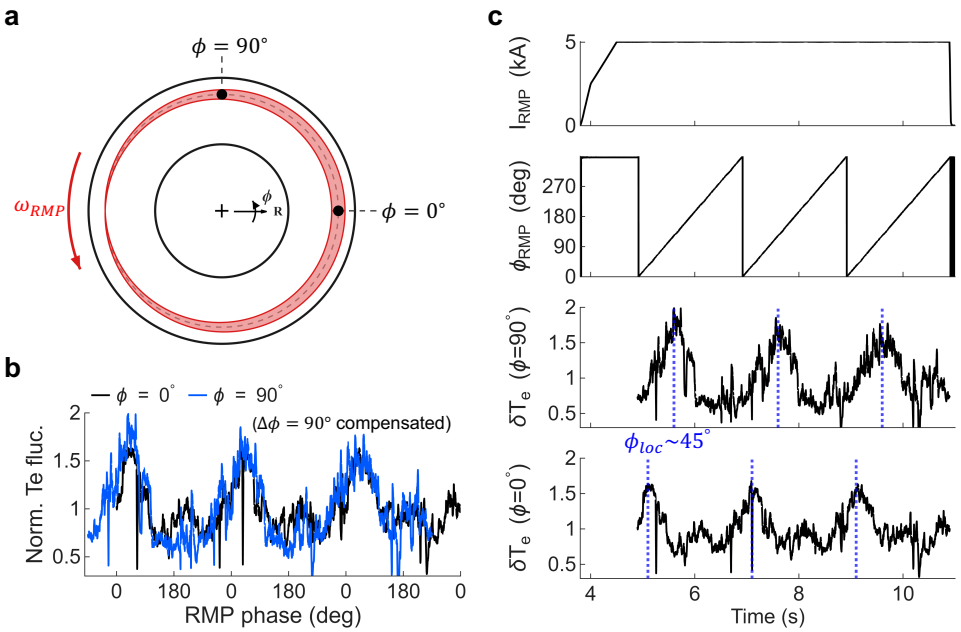
Author contributions

S.M.Y., S.K.K. and J.-K.P. jointly conceived and led the KSTAR RMP experiments and developed the central physical interpretation. S.M.Y. led the experimental data analysis and integrated the main experimental results. S.K.K. led the JOREK simulations and nonlinear MHD analysis. S.M.Y. and S.K.K. worked closely to define the key experiment–simulation comparisons and to connect the experimental observations with the nonlinear simulations. S.M.Y., S.K.K., J.-K.P., Y.M.J. and G.Y.P. contributed to the design and planning of the KSTAR experiments. Y.M.J. and G.Y.P. supported the experimental concept and KSTAR operation. J.L. and M.J.C. provided the ECE imaging measurements and contributed to the interpretation of results. J.L. performed the mode-number analysis. M.J.C. shared analysis codes and advised on ECE imaging analysis. J.W.K. provided the BES measurements and helped validate the BES analysis. J.K.L. and W.H.K. provided and interpreted the charge-exchange spectroscopy measurements. G.J.C. and T.S.H. contributed to the interpretation of turbulence and nonlinear energy transfer. Q.H. contributed to isalnd modelling, data analysis and physical interpretation. S.K. performed gyrokinetic simulations to assess the possible role of micro-instabilities. H.J. and J.Y. contributed to discussions of the broader physical context and implications of the results, including their possible relevance to space plasmas. Y.-S.N. provided helpful discussions on the broader context and presentation of the work. N.C.L. contributed to the interpretation of three-dimensional plasma response and RMP physics. S.M.Y., S.K.K. and J.-K.P. prepared the manuscript with input from all authors. A.B., R.M. and J.A.S. contributed to the interpretation and presentation of the results, supported the development of the work, and reviewed the manuscript. All authors discussed the results and reviewed the manuscript.

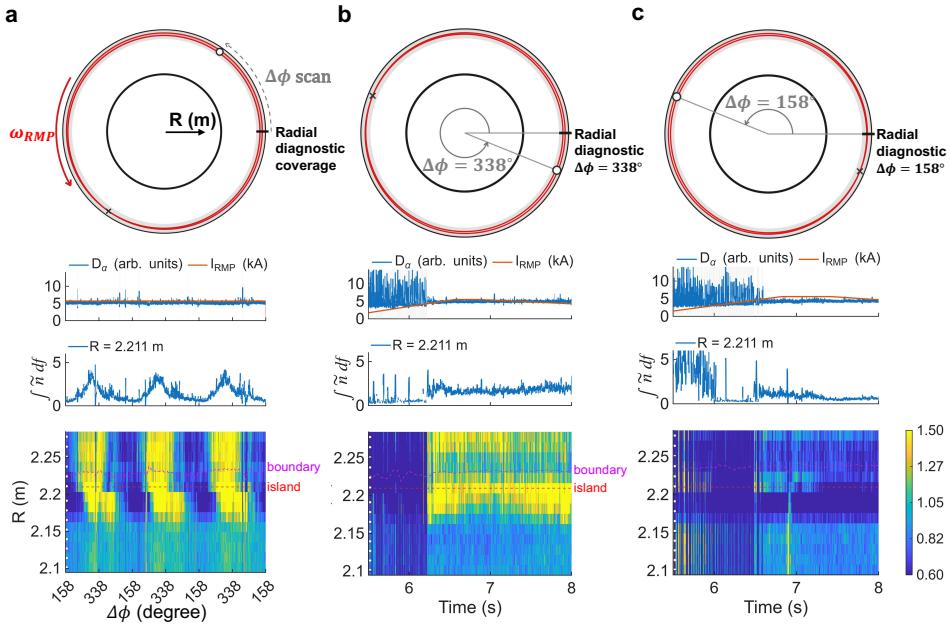
Competing interests

The authors declare no competing interests.

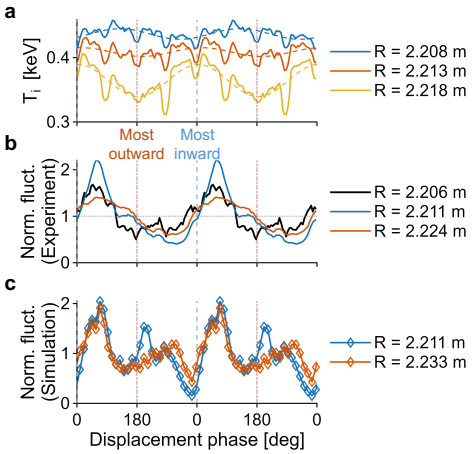
Extended Data Figures



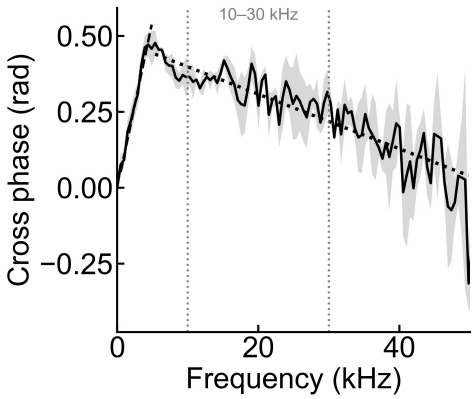
Extended Data Fig. 1 Signals at different locations around the torus appear at the same phase of the rotating applied perturbation. a, Schematic of a rotating RMP perturbation and two toroidally separated diagnostic views (black dots). **b,** Normalized band-averaged T_e fluctuation amplitude, averaged over the 1–30 kHz frequency band, measured at two toroidal locations ($\phi = 0°$ and $\phi = 90°$) plotted versus the applied RMP phase. A toroidal phase offset ($\Delta\phi = 90°$) is applied to map the two measurements into the same local phase reference, revealing a reproducible phase-dependent modulation over multiple rotations. **c,** Time traces of applied RMP current I_{RMP}, and RMP phase ϕ_{RMP}, together with δT_e at the two toroidal views. Although peak times differ between views, the peaks align when referenced to the same local RMP phase ϕ_{loc} (blue dashed markers), demonstrating that the response is locked to the rotating RMP phase.



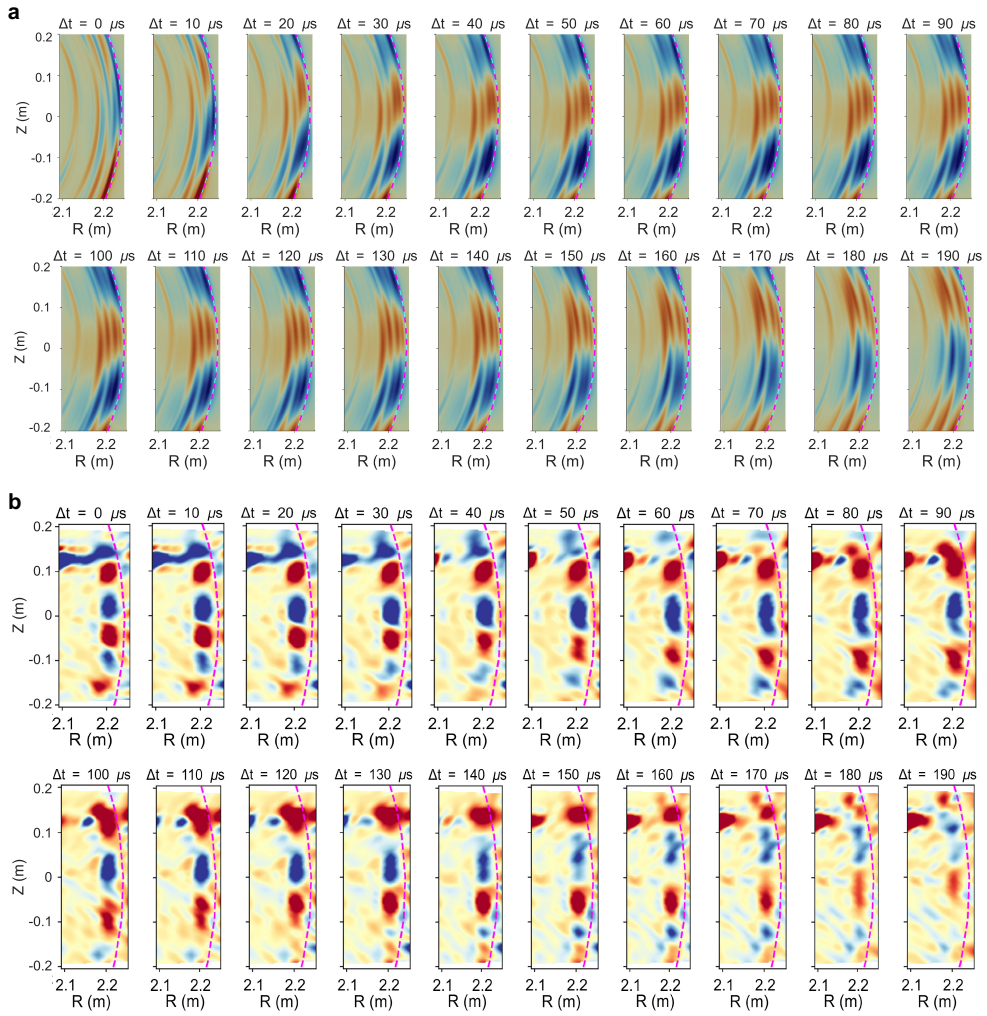
Extended Data Fig. 2 Viewing-angle dependence of edge fluctuation signatures associated with RMP ELM suppression. a, Phase scan of the mean edge density fluctuation level measured by BES in the ELM-suppressed state. $\Delta\phi$ is the toroidal angle difference between the BES view and the applied perturbation. The fluctuation level is averaged over the rotating-RMP interval and over 1–30 kHz. White dots mark the BES measurement locations. **b,c,** BES measurements at $\Delta\phi = 23°$ and $203°$ while the perturbation current is slowly increased through the transition to ELM suppression. The fluctuation signature is clear at some viewing angles but weak or not apparent at others. Some residual peak-like features remain, reflecting imperfect exclusion of transient events and measurement noise.



Extended Data Fig. 3 Phase-resolved edge response relative to radial displacement. **a,** Phase-folded CES T_i at three radial locations. **b,** Phase-folded normalized 1−30 kHz broadband fluctuation amplitudes from experiment. BES n_e fluctuations, shown in blue and orange, provide the radial comparison because they were measured at the same toroidal viewing angle as the CES measurements. The black trace shows ECE T_e fluctuations at $R = 2.206$ m, at a nearly identical toroidal angle; only one ECE channel is shown owing to limited radial sampling. **c,** Phase-folded normalized 1−30 kHz JOREK T_e fluctuation, referenced to the simulated maximum radial displacement. The displacement phase is defined such that 0° and 180° denote the most inward and most outward radial displacement, respectively; dashed lines mark these phases.



Extended Data Fig. 4 Local phase variation across the ECEI array. The cross-phase was calculated between poloidally nearest-neighbour ECEI channels to estimate how the fluctuation phase changes locally across the measurement array. The response was separated into 0−5 kHz and 5−50 kHz ranges, revealing two different trends in the frequency–phase structure. The higher-frequency trend covers the 10−30 kHz range analysed in Fig. 3a, providing a local guide to the relation between frequency and projected spatial scale.



Extended Data Fig. 5 RMP-locked oscillatory structure in $\delta T_e/\langle T_e \rangle$ in simulation and experiment. a, Nonlinear MHD simulation (JOREK) showing the spatiotemporal evolution of a localized oscillatory structure in an ELM-suppressed state. **b,** Experimental measurement showing the same phase-locked behaviour over a comparable time interval during sustained ELM suppression, beginning at $t = 7.800046$ s. In both cases, the structure is locked to the applied RMP and exhibits alternating downward and upward poloidal propagation, rather than continuous rotation in a single direction. In the experiment, the same behaviour persists over a much longer interval. The colour scale spans -0.7 to 0.7, emphasizing qualitative behaviour rather than exact amplitude agreement. See Supplementary Video 1.

Supplementary Files

This is a list of supplementary files associated with this preprint. Click to download.

- SIGuide.docx
- SupplementaryVideo1.mp4